Calibration of end-debonding strength model for FRP-reinforced masonry

Francesca Giulia Carozzi, Pierluigi Colombi *, Carlo Poggi

Department of Architecture, Built Environment and Construction Engineering (ABC), Politecnico di Milano (building 5), piazza L. da Vinci, 32, 20133 Milan, Italy

1. Introduction

Fiber Reinforced Polymer (FRP) materials are usually adopted for the strengthening of masonry structures. In particular, masonry structures are scarcely resistant to horizontal load and so highly vulnerable to seismic actions. Conventional retrofitting techniques have proven to be complex, time expensive, add considerable mass to the structures and often could not be adapted to masonry structures. In the last years the use of FRP materials as reinforcements instead of conventional methods seems then a suitable solution for the seismic upgrading. FRP strengthening systems can be conveniently used to increase the capacity of panels, arches and vaults, to wrap columns in order to increase their strength and ductility, for floor stiffening to act as a stiff diaphragm, to wrap buildings at floor and roof level etc. These materials present, in fact, good mechanical properties, rapid installation and lightness and could be applied on different substrates (clay bricks and natural stones). On the other hand the drawbacks are related to the poor behavior of epoxy resin at elevated temperatures and the durability of the bond under environmental actions (water, moisture, thermal cycling etc.) [1,2]. Finally it should be pointed out that the un-reversibility of these installations and the penetration of the primer in the substrate [3,4] pose some problems to the use of FRP systems for the strengthening of ancient masonry structures.

1.1. Problem statement

The most critical phenomenon influencing the effectiveness of the FRP repair of masonry structures is debonding of the reinforcing system from its substrate [5]. In most real situations and experimental texts, the performances of the strengthened structural elements have been limited by the debonding (at the reinforcement end or along the reinforcement) of the FRP reinforcement from the substrate. Debonding is also a very brittle phenomenon, so the bond between the FRP and the substrate should be properly designed. For this reason the bond strength evaluation is very important from the design point of view and involves the definition of a specific analytical model and experimental procedures in order to calibrate the relevant coefficients [6]. These calibrations should also be performed for different substrates (clay bricks and natural stones), reinforcement types (pultruded strips or textiles) and reinforcement materials (glass, carbon and aramid fibers). Besides, the environment effect of the bond behavior must be taken into account. It was in fact proven in the literature that the bond between the reinforcement and the substrate is sensitive to water, moisture and thermal cycling. In the revised version of the CNR-DT 200 R1/2013 guideline [7] for the design and construction

* Corresponding author.
E-mail address: pierluigi.colombi@polimi.it (P. Colombi).

Nomenclature

δ	interfacial slip
u_s,u_f	substrate and reinforcement longitudinal displacement
N_s,N_f	substrate and reinforcement axial force
A_s,A_f	substrate and reinforcement cross sectional area
ε_f	reinforcement longitudinal strain
F_{max}	maximum experimental transferable load
τ,τ_{max}	tangential and maximum tangential stress at the interface
E_s,E_f	substrate and reinforcement Young's modulus
δ_u	ultimate interfacial slip
k_b,k_G	reinforcement width and fracture energy corrector factor
Γ_F	mode II fracture energy
f_{cm},f_{ctm}	compressive and tensile strength of the clay brick substrate
b_f,b_s	reinforcement (bond) and substrate width
β_1	bond length corrector factor
l_b,l_e	bond and effective bond length
t_f	reinforcement thickness

Subscript

f	reinforcement
s	substrate
a	adhesive layer

Acronyms

FRP	Fiber Reinforced Polymer
CFRP	Carbon Fiber Reinforced Polymer
DIC	Digital Image Correlation

of externally bonded FRP strengthening systems for masonry structures, models were proposed for the bond strength and the relevant environmental conversion factors. Anyway, a refined debonding model is needed and additional experimental tests are required in order to achieve a refined calibration of the pertinent parameters.

1.2. Scope of the research

In this study the bond strength of the Carbon Fiber Reinforced Polymers (CFRP) reinforcement applied on a clay brick substrate is investigated. The reinforcement was realized by carbon textiles impregnated and bonded by epoxy resin. No other kind of substrate (e.g. natural stone), reinforcement type (e.g. pultruded strips) and reinforcement material (e.g. glass or aramid fibers) were considered in this work. Double lap push–pull shear tests were performed. In the specimen set-up, no specific surface preparation and primer application was implemented in order to increase the surface roughness and to promote the bond between the reinforcement and the substrate. Strains distributions on the reinforcement surface were collected during the tests by means of electric strain gauges. Digital Image Correlation (DIC) technique was also implemented in order to investigate qualitatively the strains field. Analytical models [8] are then proposed to investigate the load transfer mechanism and to estimate the relevant bond strength of the reinforcement system. The reinforcement strain and shear stress distribution in the adhesive layer was evaluated from the load transfer model and compared to experimental data. Besides, an enlarged experimental database for the bond strength was constructed by adding the achieved experimental results to the ones selected from the literature. This enlarged database was used to statistically estimate the coefficients of the proposed analytical model. The effect of bond length and width was also enucleated and used to validate the analytical outcomes. Finally, no attempt was performed in order to investigate the effect of environmental condition on bond strength.

1.3. Previous studies

In the last 20 years several research studies were dedicated to the investigation of the effectiveness of the strengthening of reinforced concrete structures by FRP systems. On the other hand a limited amount of research activities were dedicated to the investigation of the efficacy of FRP materials for the strengthening of steel or masonry structures. With a specific reference to the bond strength between the FRP reinforcement and the masonry substrate, experimental campaigns were carried out to investigate the debonding load and the effective length of single brick reinforced with CFRP materials [9–12]. The strain and stress distributions were generally recorded by means of electric strain gauges located on the reinforcement surface. In [11] an analytical model was also proposed and validated through experimental data for the shear stress – interfacial slip behavior at the reinforcement/substrate interface. A wide experimental campaign was recently illustrated in [13]. Single and double lap push–pull shear tests were performed on clay bricks reinforced with different composite materials (steel, carbon, glass and basalt). Recently, Ceroni et al.[14] collected experimental data from the literature in order to calibrate the coefficient used in the Italian guideline CNR DT200 R1/2013 [7] to calculate the fracture energy and the maximum load. Different set-ups were proposed in the literature to evaluate the bond strength between the substrate and the reinforcement. The most commonly used are the single and double lap push–pull shear test set-ups. In Valluzzi et al. [13] it was showed that the results of these two experimental set-ups are comparable, while other experimental studies and numerical analyses [15] demon-strated that the test set-up could strongly influence the debonding strength and the failure mode.

2. Experimental program

In this section the results of an experimental program carried out at the Materials Testing Laboratory of the Politecnico di Milano are presented. In particular, a series (28 specimens) of double lap push–pull shear tests on carbon textiles applied to the top/bottom faces of a single brick were performed. Different bond lengths (50, 100, 150, 180 and 200 mm), bond widths (30, 40, 50 and 60 mm) and substrate compressive strengths (70 MPa and 30 MPa) were considered in order to investigate the effect of these parameters on the bond strength. The double lap push–pull shear test configuration was selected due to its symmetry and to avoid additional flexural moment and peeling stresses related to un-symmetric set-up.

2.1. Materials

The reinforcement system was constituted of carbon textiles and two-components structural epoxy resin. Uniaxial tensile tests were performed on five coupons of carbon textile in order to investigate the tensile strength and the Young's modulus. Tests were carried out according to ASTM D3039 [18] using a servo-hydraulic testing machine with a load cell axial capacity of 100 kN. In order

to avoid local damage of the specimens and slip phenomena during the tensile tests, cardboard tabs were placed at the ends of the textile. The experimental results are summarized in Table 1.

Uniaxial tensile tests were carried out on three coupons in order to characterize the mechanical properties of the epoxy resin. Tests were performed under displacement control according to ASTM Standard D638 [19] using a servo-hydraulic testing machine with a load cell axial capacity of 250 kN. An extensometer was set at the full gauge length of the specimen to determine the Poisson's ratio. The experimental results are summarized in Table 2.

Two clay brick types of dimensions equal to 250 × 120 × 55 mm (length × height × thickness) were used in the experimental campaign, in order to investigate the influence of the mechanical properties of the substrate on the bond strength and the failure modes. For the first brick type (Brick_1), compression and tensile strength, elastic modulus and water absorption were experimentally determined [16] according to [20–23], while for the second one (Brick_2) just the compressive strength was investigated. The experimental results are summarized in Table 3. The two clay brick types show quite different average compressive strength, equal to 68.87 MPa and 30.26 MPa, in order to investigate the effect of this parameter on the debonding strength.

2.2. Test set-up and specimens preparation

Experimental tests (Fig. 1) were performed on double lap push–pull joints realized with a carbon textile and an epoxy matrix. The reinforcements were bonded to the two sides of a single brick. This work represents a part of a more complex experimental program developed at Politecnico di Milano with different reinforcement materials [16,17].

The reinforcements were bonded to two opposite brick surfaces without any specific preparation of the substrate. The surfaces were, in fact, simply air cleaned in order to remove incoherent particles and no specific treatment were performed to increase the surface roughness. No primer was applied to promote the adhesion. The epoxy adhesive was then distributed on the brick surfaces and the reinforcement was laid on the adhesive layer and finally the carbon textile was impregnated and pressed. The adopted bonding procedure represents the worst on site situation and it was selected since it gives conservative estimation of the debonding failure load.

A testing machine with the ultimate capacity of 250 kN was used and the tests were performed in displacement control. A supporting rig with a spherical joint was designed and realized to guarantee the correct position of the specimen and avoid the possible misalignments of the applied load (Fig. 2a).

The alignment between the specimen and the loaded end should be ensured since when the force is not perfectly aligned, flexural moment may generate peeling stresses at the reinforce-ment-to-substrate interface and then premature debonding. A spherical joint was used to this purpose. Furthermore, in order to guarantee equal loading of the two composite strips, the textile was place around a steel cylinder with a diameter equal to the dis-tance between the two textile strips. Two Teflon sheets were used to minimized friction between the carbon textile and the steel cylinder. Different bond lengths (50, 100, 150, 180 and 200 mm) and widths (30, 40, 50 and 60 mm) were considered in order to investigate the effects of these geometrical parameters on the debonding strength. As stated above, two different clay brick substrates were considered in order to investigate the effect of the brick mechanical properties on the debonding load. In particular, 21 experimental tests were performed with an high substrate average compressive strength (68.87 MPa) and 7 with a medium one (30.26 MPa). The main features characterizing the experimental response of the reinforced bricks are summarized in Table 4.

Specimen labels are as follow. The first 2 letters indicate the brick type (S1 for the Brick_1 type and S2 for the Brick_2 type). The next number indicates the bond length while the subsequent number refers to the bond width. Eventually, the specimen number is designed by the final digit. As an example, S1-50-60_1 indicates the first tested specimen realized by using Brick_1 type with a bond length of 50 mm and a bond width of 60 mm.

2.3. Recording equipment

Two LVDTs were installed on each specimen in order to monitor the experimental tests. The transducers were positioned on the brick and reinforcement surface as showed in Fig. 2b. They were located as close as possible to the reinforcement end in order to control the onset of the interfacial debonding.

Two different techniques were used to analyze the reinforcement longitudinal strain of some experimental tests. The first one involved the use of strain gauges while for the second one the DIC technique was used. Four strain gauges were installed along the reinforcement of four specimens type S1-150-60. They were located in the mid-span and in the upper part of the rein-forcement at a distance of about 10 mm. The strain gauges layout

Table 1
Mechanical characterization of carbon textile.

	Tensile strength [MPa]	Young's modulus E_f [GPa]	Elongation at failure [%]
Average	1595.8 (5)	240.4 (5)	1.43 (5)
Co.V. [%]	3.18	10.5	15.2

Note: within brackets # of samples.

Table 2
Mechanical characterization of epoxy matrix.

	Young's modulus E_a [GPa]	Poisson coefficient v [−]	Tensile strength [MPa]	Elongation at failure [%]
Average	12.84 (3)	0.29 (3)	30.20 (3)	0.358 (3)
Co.V. [%]	9.89	7.78	3.73	12.12

Note: within brackets # of samples.

Table 3
Mechanical characterization of bricks.

	Sample	E_s [GPa]	Compressive strength f_{cm} [N/mm^2]	Tensile strength f_{ctm} [N/mm^2]	Coeff. of water absorption [kg/m^{2}min]	Pull-off strength [MPa]
Standard		UNI EN 14580	UNI EN 772–1	EN 12390–6	UNI EN 1015–18	UNI EN 1542
Average	Brick_1	12.33 (4)	68.87 (12)	6.24 (3)	1.37 (6)	3.07 (12)
Standard deviation		6.18	4.23	0.84	0.37	0.23
Average	Brick_2	–	30.26 (6)	–	–	–
Standard deviation		–	1.29	–	–	–

Note: within brackets # of samples.

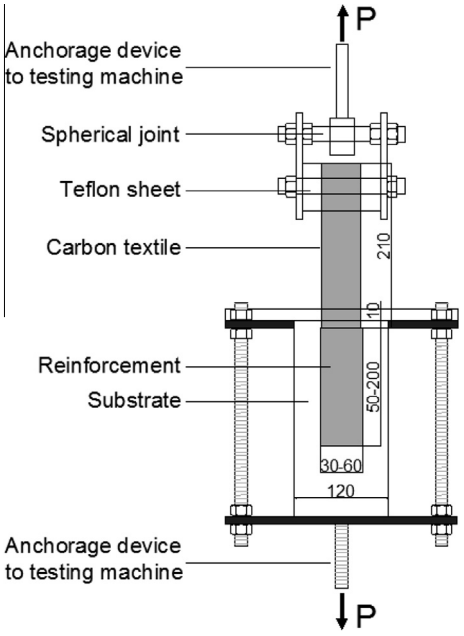

Fig. 1. Test set-up (dimensions in mm).

Table 4
Layout of experimental tests.

Sample	Substrate	Bond length [mm]	Bond width [mm]	*N.* tests
S1-50-30	Brick_1	50	30	2
S1-50-60	Brick_1	50	60	2
S1-100-40	Brick_1	100	30	2
S1-100-40	Brick_1	100	40	2
S1-100-50	Brick_1	100	50	3
S1-100-60	Brick_1	100	60	2
S1-150-60	Brick_1	150	60	8
S2–150-50	Brick_2	150	50	3
S2–180-50	Brick_2	180	50	2
S2–200-50	Brick_2	200	50	2

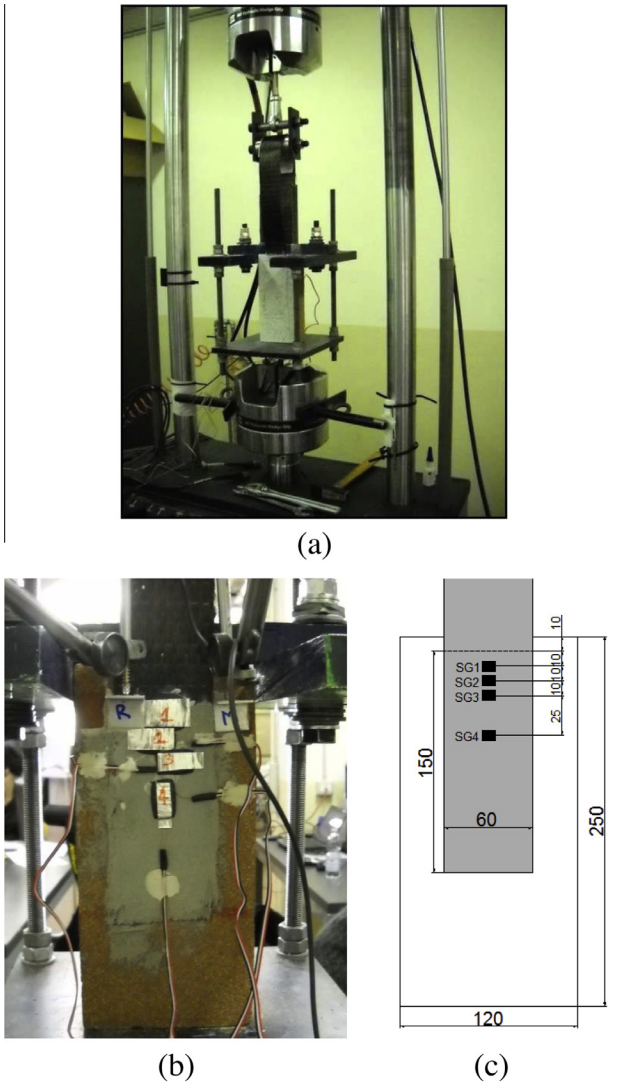

Fig. 2. Testing machine and recording equipment. (a) supporting rig (b) strain gauges and LVDTs arrangement (c) strain gauges layout (dimensions in mm).

is reported in Fig. 2c. Just few specimens were equipped with strain gauges since the main objective was to verify the load transfer mechanism.

DIC is a contactless technique which offers qualitative and quantitative information on the heterogeneous deformations of an object surface. It provides a full-field displacement over a two or three dimensional surface by comparing images of the deformed specimen surface to the un-deformed one [24]. The surface of the sample was painted with white paint and a black pattern of points (Fig. 3a). The location and the dimensions of the reference points were random. The light sources and the camera (Fig. 3b) were located near the sample surface and calibrated in order to guarantee an high degree of information content of the images.

The density distribution of the reference points should have a shape as close as possible to Gaussian. The DIC technique is, in fact, based on the maximization of a correlation coefficient that is determined by examining pixel intensity array subset on two or more corresponding images and extracting the displacement mapping function that relates the images [25].

3. Experimental results

In this section experimental results are presented in term of observed failure mode and recorded failure load.

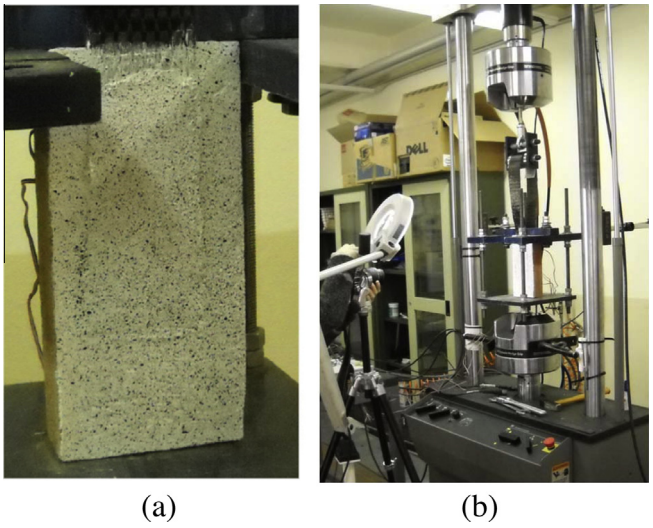

Fig. 3. DIC technique set-up. (a) specimen surface with randomly distributed reference points (b) image recording with a digital camera.

3.1. Failure mode

Failure mode was mainly due to the reinforcement debonding from the substrate with a thin brick layer attached to the reinforcement. The thickness of the brick layer was equal to few millimeters. Only in specimen type S1-50-30 a slippage of the textile was observed. The typical failure mode is reported in Fig. 4.

3.2. Failure load

Table 5 reports the maximum average failure load for each configuration. Note that the values reported in Table 5 refers to load *P* (see Fig. 1) recorded by the loading cell of the testing machine and then they are equal to two times the load *F* in the carbon textiles.

Results listed in Table 5 are, from a general point of view, coherent with the literature outcomes. First, the debonding load linearly increases with the bond width. Moreover, the higher the substrate compressive strength the higher the debonding load. Finally, the effective bond length for low brick compressive strength appears to be approximately equal to 150 mm while for high substrate compressive strength it seems to be around 100 mm.

Figs. 5a and b and 6 report the load–displacement curves as recorded by the testing machine (load cell and stroke displacement).

In these two figures, just the tests for the substrate "Brick-1" with a bond width of 60 mm (12 tests) and a bond length of 100 mm (9 specimens) and the tests with substrate "Brick-2" (7 tests) were reported. Note again that the values showed in Figs. 5 and 6 refers to the load *P* recorded by the loading cell of the testing machine and then they are equal to two times the load *F* in the carbon textiles (see Fig. 2). The load–displacement curves in Figs. 5 and 6 exhibit a linear behavior up the maximum debonding load followed by a sudden drop of the applied load.

4. Analytical models

In this section two analytical models are presented. The first one investigates the load transfer mechanism between the reinforcement and the substrate while the second model analyzes the reinforcement bond strength and provides an estimation of the debonding load.

4.1. Load transfer model

In the model to investigate the load transfer mechanism between the substrate and the reinforcement the following assumptions are made:

1. Substrate and reinforcement are homogeneous and linear elastic.

Fig. 4. Typical failure mode.

Table 5
Average test results (mean value at debonding load recorded by the testing machine).

Length [mm]	Width [mm]			
	30	40	50	60
50	10.11 kN*	–	–	21.26 kN*.
100	15.32 kN*	12.95 kN*	21.04 kN*.	28.11 kN*
150	–	–	14.10 kN**	21.11 kN*
180	–	–	12.99 kN**	–
200	–	–	12.17 kN**	–

* Sample prepared with Brick_1.
** Sample prepared with Brick_2.

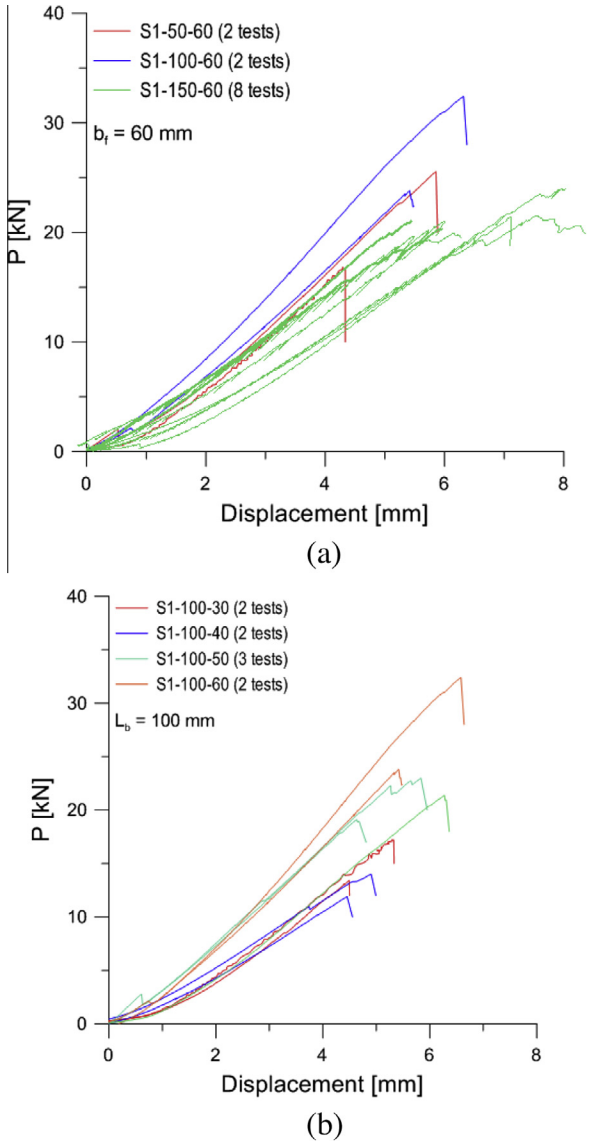

Fig. 5. Load–displacement curves for debonding tests. (a) bond length of 50, 100 and 150 mm and width of 60 mm (brick-1) (b) bond length of 100 mm and width of 30, 40, 50 and 60 mm (brick-1).

2. Linear kinematic relationships for the substrate and the reinforcement.
3. Interfacial linear ascending with a sudden drop bond-slip relationship.
4. Adhesive layer is subjected to constant shear stress across the thickness.
5. Normal (peeling stress) in the adhesive layer are not taken into account.

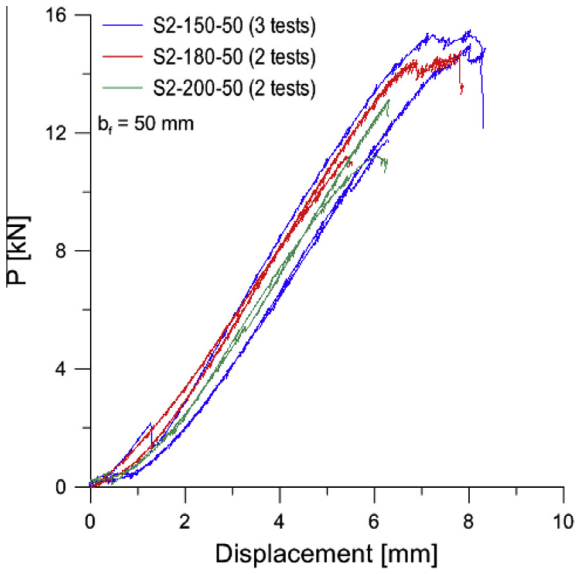

Fig. 6. Test results of specimens with bond length of 150, 180 and 200 mm, and width of 50 mm (brick-2).

6. Bending effect are neglected.

The push–pull scheme adopted in the model is shown in Fig. 7.

The interfacial slip is defined as the relative longitudinal displacement between the reinforcement and the substrate.

$$\delta = u_f - u_s \tag{1}$$

where u_f and u_s are the reinforcement and substrate longitudinal displacement, respectively. The local equilibrium in the reinforcement in the longitudinal direction reads (see Fig. 7):

$$\frac{1}{b_f}\cdot\frac{dN_f}{dx} - \tau = 0 \tag{2}$$

where N_f is the reinforcement axial force, b_f is the reinforcement width and τ is the tangential stress in the adhesive layer.

The global equilibrium (see Fig. 7) in the longitudinal direction states:

$$N_s + 2N_f = 0 \tag{3}$$

where N_s is the substrate axial force. According to assumptions 1–3, the constitutive relationships for the reinforcement, the substrate and the interface are:

$$N_f = A_f E_f \varepsilon_f = A_f E_f \frac{du_f}{dx} \tag{4}$$

$$N_s = A_s E_s \varepsilon_s = A_s E_s \frac{du_s}{dx} \tag{5}$$

$$\tau = \frac{\tau_{max}^2}{2\Gamma_F}\delta \tag{6}$$

where A_f and A_s are the reinforcement and substrate sectional area, respectively, ε_f and ε_s are the reinforcement and substrate longitudinal strain while E_f and E_s are the reinforcement and substrate Young's modulus. As per assumption 3, the shear stress-slip relationship is assumed linear up to the maximum allowable interfacial shear stress, τ_{max}, that is, before the occurrence of interfacial fracture (see Fig. 7). The shear stress is then assumed to suddenly drop to zero when the value of the slip exceeds δ_u without consideration of the softening behavior. The shear stress-slip relationship in Eq. (6) is function of the mode II fracture energy Γ_F which is defined as the energy required for local bond fracture and is represented by the area under the shear stress-slip curve (see Fig. 7). This is a simplified interface behavior but it produces meaningful results in term of maximum transferable load by the carbon textiles, $F_{max} = P_{max}/2$, and effective bond length, l_e. Inserting Eqs. (3)–(6) into Eq. (2) one has:

$$\frac{d^2\delta}{dx^2} - \frac{f_2}{f_1}\delta = 0 \tag{7}$$

$$f_1 = \frac{2\Gamma_F}{b_f\tau_{max}^2} \tag{8}$$

$$f_2 = \frac{2}{E_s A_s} + \frac{1}{E_f A_f} \tag{9}$$

Defining $\lambda^2 = \frac{f_2}{f_1}$ one finally obtains the following second order differential equation for the interfacial slip δ:

$$\frac{d^2\delta}{dx^2} - \lambda^2\delta = 0 \tag{10}$$

$$\lambda^2 = \frac{b_f\tau_{max}^2}{2\Gamma_F}\left(\frac{2}{E_s A_s} + \frac{1}{E_f A_f}\right) \tag{11}$$

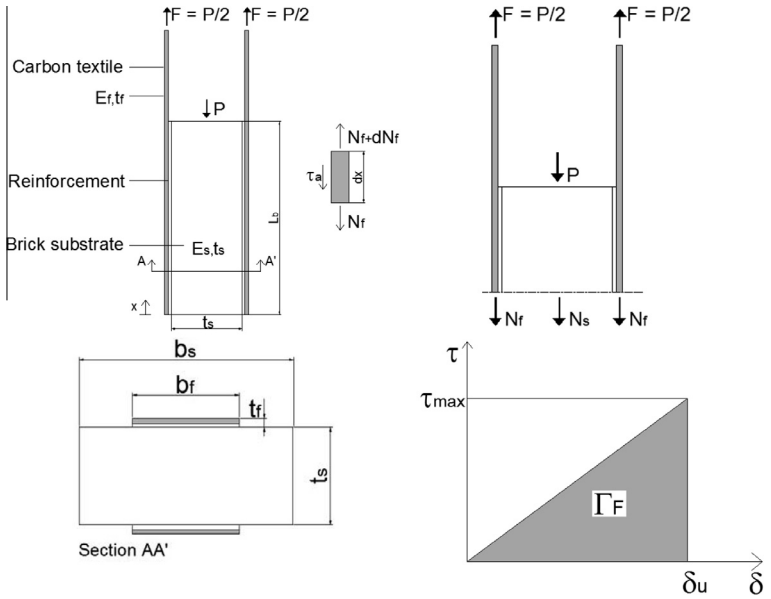

Fig. 7. Push–pull scheme.

with the boundary conditions at the lower ($x = 0$) and upper ($x = l_b$) reinforcement ends:

$$N_f = \frac{1}{f_2}\frac{d\delta}{dx} = 0 \quad \text{at } x = 0 \tag{12}$$

$$N_f = \frac{1}{f_2}\frac{d\delta}{dx} = \frac{P}{2} \quad \text{at } x = l_b \tag{13}$$

The expression for the interfacial slip is:

$$\delta = \frac{P \cdot f_2}{2\lambda \sinh(\lambda l_b)} \cosh(\lambda x) \tag{14}$$

The longitudinal strain in the reinforcement layer is equal to:

$$\varepsilon_f = \frac{P}{2A_f E_f} \cdot \frac{\sinh(\lambda x)}{\sinh(\lambda l_b)} \tag{15}$$

while the tangential stress on the interface is given by:

$$\tau = \frac{P \cdot \lambda}{2b_f} \cdot \frac{\cosh(\lambda x)}{\sinh(\lambda l_b)} \tag{16}$$

Fig. 8 shows the interfacial slip distribution at different load levels obtained by the analytical model (Eq. (14)) for specimen type S1-150-60.

4.2. Bond strength model

The evaluation of the maximum transferable load by the carbon textiles, F_{max}, requires the definition of a reliable interfacial bond-slip model. Different models were studied in the last years with reference to different substrates (in particular concrete and steel). Lu et al. [27] summarized different existing bond-slip models for adhesive interface of a FRP-to-concrete. As stated above, in the proposed load transfer model a linear ascending model with a sudden drop bond-slip is adopted. Failure (debonding) is achieved when the interfacial shear stress at the upper reinforcement end ($x = l_b$) is equal to the local bond strength τ_{max}. Based on the shear stress distribution provided by Eq. (16), the maximum transferable load, F_{max}, can be calculated as:

$$F_{max} = \frac{\tau_{max} \cdot b_f}{\lambda} \cdot \tanh(\lambda l_b) \tag{17}$$

For large values of the bond length, l_b, Eq. (17) reduces to:

$$F_{max} = \frac{\tau_{max} \cdot b_f}{\lambda} \tag{18}$$

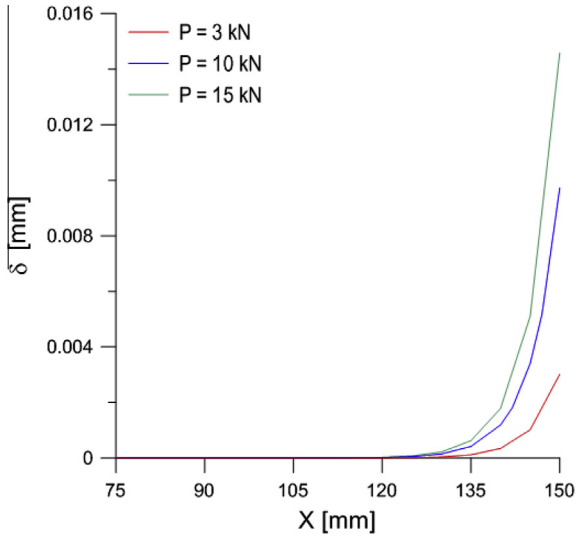

Fig. 8. Interfacial slip distribution for different load levels.

If $E_s A_s \gg E_f A_f$ one has from Eq. (11):

$$\lambda = \frac{\tau_{max}}{\sqrt{2\Gamma_F E_f t_f}} \tag{19}$$

and then the following expression is obtained for F_{max}:

$$F_{max} = b_f \sqrt{2\Gamma_F E_f t_f} \tag{20}$$

Despite the adopted simplified bond-slip model (see Eq. (6)), the expression for the maximum transferable load given in Eq. (20) is the usual one adopted in the literature.

The effective bond length, l_e, is usually defined as the bond length needed to transfer 97% of the maximum transferable load. One has then from Eq. (17) $\tanh(\lambda l_e) = 0.97$ and finally:

$$l_e = \frac{2}{\lambda} \tag{21}$$

Eq. (20) provides a rather conservative estimation of the effective bond length and it is sometime adopted in the literature [27].

The mode II fracture energy Γ_F is defined as the area under the bond-slip relationship (see Fig. 8).

$$\Gamma_F = \int_0^\infty \tau dx = \frac{1}{2}\tau_{max}\delta_u \tag{22}$$

The evaluation of the fracture energy requires the evaluation of the maximum tangential stress at the interface, τ_{max}, and the ultimate interfacial slip, δ_u. In [7], a value δ_u = 0.4 mm is suggested for the ultimate interfacial slip. In [8,14], the Mohr–Coulomb failure crite-rion is used to determine the value of τ_{max}. The following expression was suggested for the maximum tangential stress at the interface:

$$\tau_{max} = \frac{1}{2}\sqrt{f_{cm} f_{ctm}} \tag{23}$$

where f_{cm} and f_{ctm} are the compressive and tensile strength of the masonry substrate.

The mode II fracture energy, Γ_F, is then evaluated from Eq. (22) as:

$$\Gamma_f = \frac{1}{4}\delta_u \sqrt{f_{cm} f_{ctm}} \tag{24}$$

The maximum transferable load is finally evaluated, for a bond length greater than the effective bond length (see Eq. (21)), inserting Eq. (24) in Eq. (20). However, in the developed theoretical model the width effect was not taken into account. In practical applications, in fact, the reinforcement width is smaller than the substrate one. In the literature a geometric corrector factor k_b is then introduced in Eq. (23) in order to take into account the real stress distribution in the substrate and the three-dimensional effect of shear transfer. The following expression is suggested in [7]:

$$k_b = \sqrt{\frac{3 - \frac{b_f}{b_s}}{1 + \frac{b_f}{b_s}}} \tag{25}$$

where b_f and b_s are the reinforcement and substrate width, respectively. Additionally, fracture (debonding) occurs in an inhomogeneous zone due to the mix of the substrate and adhesive. The material properties of the interfacial zone cannot be evaluated experimentally and then a corrector factor, k_G, to be calibrated experimentally, is required in Eq. (24). The final corrected expression of the mode II fracture energy, Γ_F, is then:

$$\Gamma_f = \frac{1}{4}k_b k_G \delta_u \sqrt{f_{cm} f_{ctm}} \tag{26}$$

If the bond length is lower than the effective one, an additional correction factor, β_1, has to be introduced. This takes into account the influence of the bond length l_b, and is defined in [7] as:

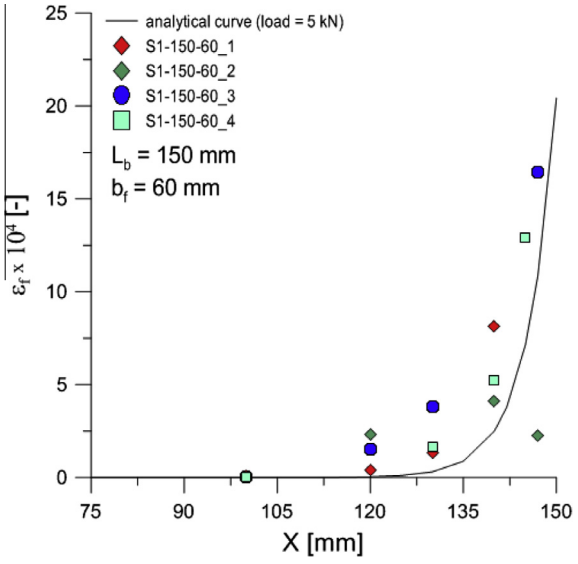

Fig. 9. Reinforcement longitudinal strain distribution: analytical and experimental results for a load level equal to 5 kN.

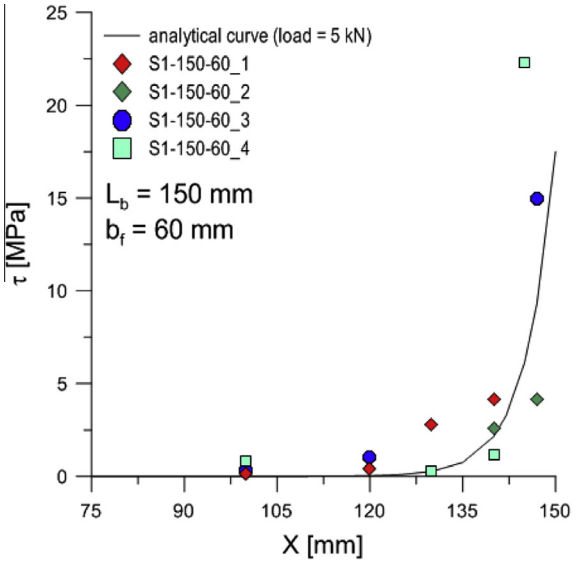

Fig. 10. Interfacial shear stress distribution: analytical and experimental results for a load level equal to 5 kN.

$$\beta_1 = \frac{l_b}{l_e}\left(2 - \frac{l_b}{l_e}\right) \tag{27}$$

Eq. (27) is effective for $l_b/l_e < 1$ while for $l_b/l_e > 1$ the value cor-responding to $l_b/l_e = 1$ is used. The corrected expression for the max-imum transferable load, F_{max}, is then:

$$F_{max} = \beta_1 b_f \sqrt{2\Gamma_F E_f t_f} \tag{28}$$

where the mode II fracture energy, Γ_F, is given by Eq. (26).

The effective bond length, l_e, is provided by Eq. (21). However, this formula was derived under the assumption of a linear bond-slip relationship (see Fig. 8). If a bilinear bond-slip model is used [27], one has $\sin(\lambda l_e) = 0.97$ and then:

$$l_e = \frac{\pi}{2\lambda} \tag{29}$$

which provides a less conservative estimation of the effective bond length. Inserting Eq. (19) into Eq. (29), the following expression for the effective bond length is obtained:

$$l_e = \frac{1}{\tau_{max}}\sqrt{\frac{\pi^2 E_f t_f \Gamma_F}{2}} \tag{30}$$

5. Validation of the load transfer model

In this section the results of the load transfer model are compared to the experiments in term of reinforcement longitudinal strains and bond shear stresses.

5.1. Reinforcement longitudinal strain

The longitudinal strains distribution achieved by using the load transfer model is compared in Fig. 9 to the experimental data collected for specimen type S1-150-60 by the strain gauges located on the reinforcement surface. Fig. 9 shows a good comparison between experimental and analytical results.

5.2. Interface shear stress

The interfacial shear stress can be evaluated from the strain gauges readings. Taking into account Eqs. (2) and (4) one has:

$$\tau = \frac{E_f \cdot A_f}{b_f}\frac{d\varepsilon_f}{dx} \tag{31}$$

The first derivative of the longitudinal reinforcement strain can be approximated by the secant method as follow:

$$\frac{d\epsilon_f}{dx} = \frac{\varepsilon_f^{i+1} - \varepsilon_f^i}{x^{i+1} - x^i} \tag{32}$$

and then the interfacial shear stress between two consecutive strain gauges is given by:

$$\tau = \frac{E_f A_f(\varepsilon_f^{i+1} - \varepsilon_f^i)}{b_f(x^{i+1} - x^i)} \tag{33}$$

In Fig. 10 the results of the bond strength model in term of interfacial shear stress for specimen type S1-150-60 are compared to experimental results. Fig. 10 shows a good comparison between experimental and analytical results.

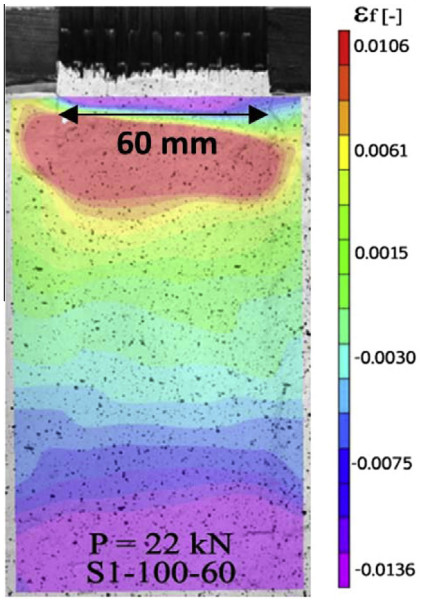

Fig. 11. Strain field from DIC technique for a load level equal to 22 kN.

Table 6
Experimental enlarged database.

Author	l_b [mm]	b_f [mm]	E_f [GPa]	f_{cm} [MPa]	f_{ctm} [MPa]	k_b	β_1	$F_{max,exp}$ [kN]	$\Gamma_{F,exp}$ [N/mm]	$k_{G,exp}$
Ceroni et al. [14]	200	50	230	19.21	1.9	1.35	1.00	6.81	0.24	0.287
	200	50	230	19.21	1.9	1.35	1.00	6.81	0.24	0.287
	200	50	230	19.21	1.9	1.35	1.00	6.81	0.24	0.287
Kwiecien [12]	200	50	230	9.9	1	1.35	1.00	5.78	0.16	0.385
	200	50	230	9.9	1	1.35	1.00	6.81	0.23	0.535
	200	50	230	9.9	1	1.35	1.00	6.69	0.22	0.516
	200	50	230	9.9	1	1.35	1.00	5.88	0.17	0.399
	200	50	230	9.9	1	1.35	1.00	6.25	0.19	0.451
Capozucca [26]	150	50	230	24.9	2.5	1.40	1.00	8.75	0.38	0.341
	180	50	230	24.9	2.5	1.40	1.00	9.02	0.40	0.362
	290	50	230	24.9	2.5	1.40	1.00	8.98	0.40	0.359
	290	50	230	24.9	2.5	1.40	1.00	9.00	0.40	0.361
	215	50	230	24.9	2.5	1.40	1.00	7.40	0.39	0.244
	230	50	230	24.9	2.5	1.40	1.00	8.25	0.39	0.303
	235	50	230	24.9	2.5	1.40	1.00	9.70	0.27	0.419
	240	50	230	24.9	2.5	1.40	1.00	8.52	0.33	0.323
	250	50	230	24.9	2.5	1.40	1.00	10.20	0.46	0.463
Caratelli et al. [13]	160	50	234	19.76	1.76	1.35	1.00	5.74	0.17	0.208
	160	50	234	19.76	1.76	1.35	1.00	5.97	0.18	0.225
	160	50	234	19.76	1.76	1.35	1.00	6.17	0.19	0.240
	160	50	234	19.76	1.76	1.35	1.00	6.62	0.22	0.277
	160	50	234	19.76	1.76	1.35	1.00	6.94	0.24	0.304
De Felice [13]	160	50	234	19.76	1.76	1.35	1.00	5.32	0.14	0.179
	160	50	234	19.76	1.76	1.35	1.00	5.60	0.16	0.198
	160	50	234	19.76	1.76	1.35	1.00	6.85	0.24	0.296
	160	50	234	19.76	1.76	1.35	1.00	7.16	0.26	0.324
	160	50	234	19.76	1.76	1.35	1.00	8.06	0.33	0.410
Kwiecien et al. [13]	160	50	234	19.76	1.76	1.35	1.00	5.69	0.16	0.204
	160	50	234	19.76	1.76	1.35	1.00	6.37	0.20	0.256
	160	50	234	19.76	1.76	1.35	1.00	7.08	0.25	0.316
	160	50	234	19.76	1.76	1.35	1.00	7.46	0.28	0.352
	160	50	234	19.76	1.76	1.35	1.00	8.35	0.35	0.440
	160	50	234	19.76	1.76	1.35	1.00	5.78	0.17	0.211
	160	50	234	19.76	1.76	1.35	1.00	5.88	0.17	0.218
	160	50	234	19.76	1.76	1.35	1.00	6.25	0.20	0..247
	160	50	234	19.76	1.76	1.35	1.00	6.69	0.23	0.283
	160	50	234	19.76	1.76	1.35	1.00	6.81	0.23	0.293
Garmenedia [13]	160	50	234	19.76	1.76	1.35	1.00	6.10	0.19	0.235
	160	50	234	19.76	1.76	1.35	1.00	6.13	0.19	0.237
	160	50	234	19.76	1.76	1.35	1.00	7.62	0.29	0.366
	160	50	234	19.76	1.76	1.35	1.00	7.89	0.31	0.393
	160	50	234	19.76	1.76	1.35	1.00	8.04	0.33	0.409
Oliveira et al. [13]	160	50	234	19.76	1.76	1.35	1.00	6.91	0.24	0.302
	160	50	234	19.76	1.76	1.35	1.00	7.72	0.30	0.376
	160	50	234	19.76	1.76	1.35	1.00	7.90	0.31	0.394
	160	50	234	19.76	1.76	1.35	1.00	8.59	0.37	0.466
	160	50	234	19.76	1.76	1.35	1.00	8.81	0.39	0.490
Leone et al. [13]	160	50	234	19.76	1.76	1.35	1.00	4.09	0.08	0.106
	160	50	234	19.76	1.76	1.35	1.00	7.36	0.27	0.342
	160	50	234	19.76	1.76	1.35	1.00	5.16	0.13	0.168
	160	50	234	19.76	1.76	1.35	1.00	6.87	0.274	0.298
Castori et al. [13]	160	50	234	19.76	1.76	1.35	1.00	4.68	0.11	0.138
	160	50	234	19.76	1.76	1.35	1.00	6.20	0.19	0.243
	160	50	234	19.76	1.76	1.35	1.00	6.732	0.23	0.286
	160	50	234	19.76	1.76	1.35	1.00	6.755	0.23	0.288
	160	50	234	19.76	1.76	1.35	1.00	7.10	0.25	0.318
Grande et al. [13]	160	50	234	19.76	1.76	1.35	1.00	5.55	0.15	0.195
	160	50	234	19.76	1.76	1.35	1.00	6.31	0.20	0.252
	160	50	234	19.76	1.76	1.35	1.00	6.645	0.22	0.279
	160	50	234	19.76	1.76	1.35	1.00	7.595	0.29	0.364
	160	50	234	19.76	1.76	1.35	1.00	7.74	0.30	0.378
Viskovic et al. [13]	160	50	234	19.76	1.76	1.35	1.00	7.74	0.30	0.379
	160	50	234	19.76	1.76	1.35	1.00	7.74	0.30	0.379
	160	50	234	19.76	1.76	1.35	1.00	7.74	0.30	0.379
	160	50	234	19.76	1.76	1.35	1.00	7.74	0.30	0.379
	160	50	234	19.76	1.76	1.35	1.00	7.75	0.30	0.379
Lignola et al. [13]	160	50	234	19.76	1.76	1.35	1.00	5.69	0.16	0.205
	160	50	234	19.76	1.76	1.35	1.00	6.48	0.21	0.266
	160	50	234	19.76	1.76	1.35	1.00	7.18	0.26	0.326

Table 6 (*continued*)

Author	l_b [mm]	b_f [mm]	E_f [GPa]	f_{cm} [MPa]	f_{ctm} [MPa]	k_b	β_1	$F_{max,exp}$ [kN]	$\Gamma_{F,exp}$ [N/mm]	$k_{G,exp}$
	160	50	234	19.76	1.76	1.35	1.00	8.19	0.34	0.424
Valluzzi [13]	160	50	234	19.76	1.76	1.35	1.00	6.97	0.24	0.307
	160	50	234	19.76	1.76	1.35	1.00	7.22	0.26	0.329
	160	50	234	19.76	1.76	1.35	1.00	7.79	0.31	0.383
	160	50	234	19.76	1.76	1.35	1.00	7.83	0.31	0.387
	160	50	234	19.76	1.76	1.35	1.00	7.89	0.31	0.393
	160	50	234	19.76	1.76	1.35	1.00	7.52	0.28	0.357
	160	50	234	19.76	1.76	1.35	1.00	7.58	0.29	0.363
	160	50	234	19.76	1.76	1.35	1.00	8.38	0.35	0.444
	160	50	234	19.76	1.76	1.35	1.00	7.59	0.29	0.364
	160	50	234	19.76	1.76	1.35	1.00	8.65	0.38	0.473
Authors	50	30	240	68.87	6.2	1.29	0.77	5.15	0.36	0.118
	50	30	240	68.87	6.2	1.29	0.77	4.97	0.34	0.110
	50	60	240	68.87	6.2	1.29	0.74	12.77	0.56	0.208
	50	60	240	68.87	6.2	1.29	0.74	8.42	0.24	0.09
	100	30	240	68.87	6.2	1.48	1.00	8.62	1.01	0.330
	100	30	240	68.87	6.2	1.48	1.00	6.71	0.61	0.200
	100	40	240	68.87	6.2	1.41	1.00	7.00	0.38	0.128
	100	40	240	68.87	6.2	1.41	1.00	5.95	0.27	0.092
	100	50	240	68.87	6.2	1.35	1.00	11.49	0.65	0.232
	100	50	240	68.87	6.2	1.35	1.00	9.55	0.45	0.160
	100	50	240	68.87	6.2	1.35	1.00	10.69	0.56	0.201
	100	60	240	68.87	6.2	1.29	1.00	16.20	0.89	0.335
	100	60	240	68.87	6.2	1.29	1.00	11.91	0.48	0.181
	150	50	240	30.26	3.0	1.38	1.00	7.51	0.34	0.215
	150	50	240	30.26	3.0	1.38	1.00	7.75	0.36	0.229
	150	50	240	30.26	3.0	1.38	1.00	5.89	0.21	0.132
	150	60	240	68.87	6.2	1.29	1.00	10.51	0.38	0.141
	150	60	240	68.87	6.2	1.29	1.00	10.15	0.35	0.131
	150	60	240	68.87	6.2	1.29	1.00	10.52	0.38	0.141
	150	60	240	68.87	6.2	1.29	1.00	9.97	0.34	0.127
	150	60	240	68.87	6.2	1.29	1.00	10.76	0.39	0.147
	150	60	240	68.87	6.2	1.29	1.00	10.73	0.39	0.146
	150	60	240	68.87	6.2	1.29	1.00	9.84	0.33	0.123
	150	60	240	68.87	6.2	1.29	1.00	11.99	0.49	0.182
	180	50	240	30.26	3.0	1.38	1.00	7.39	0.33	0.208
	180	50	240	30.26	3.0	1.38	1.00	5.61	0.19	0.120
	200	50	240	30.26	3.0	1.38	1.00	5.60	0.19	0.119
	200	50	240	30.26	3.0	1.38	1.00	6.57	0.26	0.164

Note:

l_b Bond length.
b_f Reinforcement (bond) width.
E_f Reinforcement Young's modulus.
f_{cm} Compressive strength of the substrate.
f_{ctm} Tensile strength of the substrate.
k_b Reinforcement width corrector factor.
β_1 Bond length corrector factor
$F_{max,exp}$ Experimental maximum transferable load.
$\Gamma_{F,exp}$ Experimental fracture energy .
$k_{G,exp}$ Experimental fracture energy corrector factor.

Both experimental and analytical results highlighted that only few centimeters at the upper reinforcement end are involved in the load transfer mechanism. This is confirmed from the qualita-tive point of view by the DIC analyses in Fig. 11 for specimen S1-100-60.

6. Calibration of the bond strength model

In this section the experimental campaign carried out at the Politecnico di Milano (28 experimental tests) are combined to a set of selected data from the literature (81 experimental tests) [12–14,26] in order to get an enlarged database of 109 tests results for push–pull shear tests. The criteria used to select the experimental results from the literature were:

1. Single clay brick substrate, that is, no mortar joints are considered.
2. Debonding failure mode involving a thin layer of brick substrate.
3. Reinforcement realized by using carbon textile and epoxy resin.
4. No specific surface preparation of the substrate. As showed in [9], surface preparation plays a very important role in the failure mode and recorded maximum transferable load.

Results are listed in Table 6.

Table 6 reports for each configuration the recorded experimental failure load, the clay bricks mechanical properties and the geometry and mechanical properties of the reinforcement. The equivalent reinforcement thickness was for all cases equal to 0.17 mm.

The mode II fracture energy, Γ_F, and the fracture energy coefficients, k_G, listed in Table 6 were evaluated according to Eqs. (28) and (26) as:

$$\Gamma_{F,exp} = \frac{F_{max,exp}^2}{2\beta_1^2 b_f^2 E_f t_f} \tag{34}$$

$$k_{G,exp} = \frac{4\Gamma_{F,exp}}{k_b \delta_u \sqrt{f_{cm} f_{ctm}}} \tag{35}$$

where $F_{max,exp}$ is the recorded experimental failure load. The reinforcement width corrector factor, k_b, was computed by using Eq. (25) while the bond length corrector factor, β_1, was evaluated by using Eq. (27).

Authors' results in Table 6 appear to be slightly conservative when compared to similar results from the literature. This is probably due to the adopted surfaces preparation. The decision to avoid any specific surface treatment and primer application probably led to lower debonding strength.

6.1. Statistical calibration of the bond strength model

In Table 6 the mode II fracture energy $\Gamma_{F,exp}$ was first computed from Eq. (34) and then the fracture parameter $k_{G,exp}$ was evaluated from Eq. (35). In Fig. 12, the experimental cumulative distribution function of k_G is compared to the normal and lognormal theoretical models.

The corresponding 50% and 5% percentile values were then evaluated and showed in Table 7.

It appears from Fig. 12 and Table 7 that the normal and lognormal theoretical models produce similar results but the normal one seems to fit better the experimental outputs.

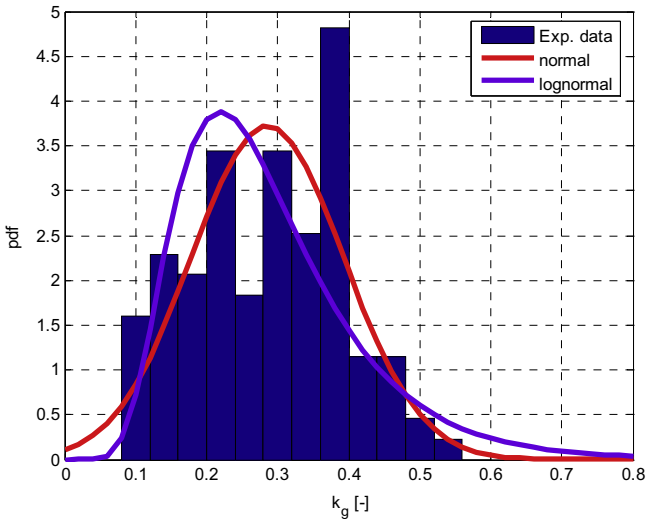

Fig. 12. Statistical distribution of k_G parameter. (a) probability density function (b) cumulative distribution function.

6.2. Bond length and bond width effects

Fig. 13 shows the experimental results for the reinforcement width corrector factor, $k_{b,exp}$, as function of the ratio between the reinforcement and substrate width, b_f/b_s. Results for $k_{b,exp}$ are evaluated from Eq. (26) as:

$$k_{b,exp} = \frac{4\Gamma_{F,exp}}{k_G \delta_u \sqrt{f_{cm} f_{ctm}}} \tag{36}$$

where k_G is the 50% percentile of the experimental mode II fracture energy corrector factor (see Table 7).

Fig. 13 shows that the adopted model for the corrector factor k_b fits well the experimental data. Fig. 14 shows the experimental

Table 7
Calibration of k_G parameter.

Distribution	5%	50%
Normal	0.109	0.285
Lognormal	0.130	0.263

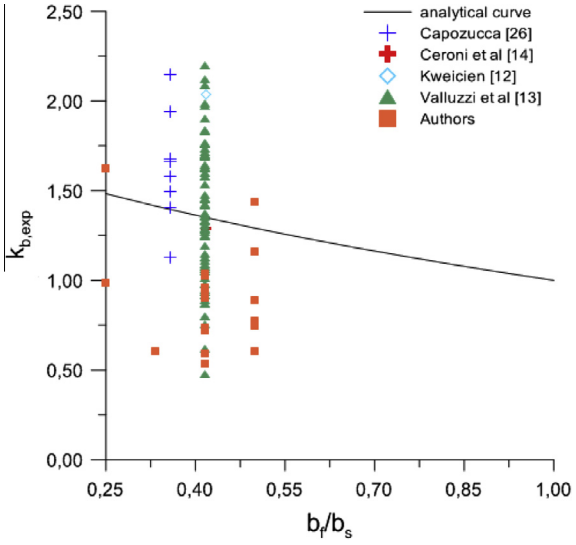

Fig. 13. Correction factor k_b.

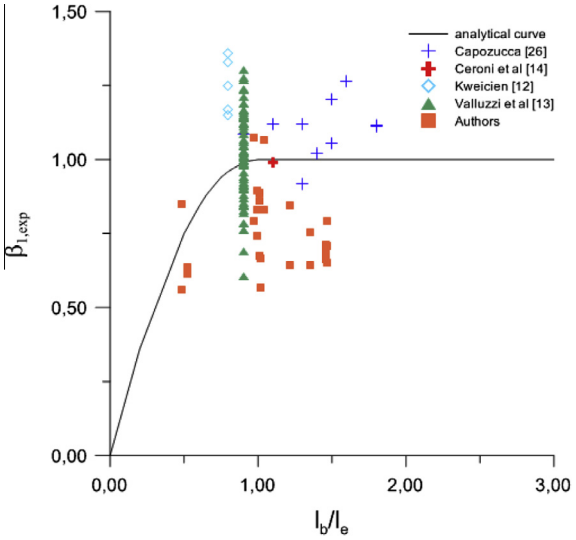

Fig. 14. Correction facto β_1.

bond length corrector factor, $\beta_{1,exp}$, as a function of the normalized bond length, l_b/l_e. The bond length is normalized with reference to the effective bond length, l_e. Results for $\beta_{1,exp}$ are evaluated from Eq. (28) as:

$$\beta_{1,exp} = \frac{F_{max,exp}}{b_f \sqrt{2E_f t_f \Gamma_F}} \tag{37}$$

where the mode II fracture energy, Γ_F, was evaluated by using Eq. (26) and the experimentally calibrated (50% percentile) fracture energy corrector factor, k_G (see Table 7).

Again, Fig. 14 shows that the adopted model for the corrector factor β_1 fits well the experimental data. In particular, the model appears to be able to capture the reduction of the debonding strength with the bond length.

7. Conclusions

In the present paper the experimental results of 28 double lap push–pull shear tests carried out on a single brick reinforced with CFRP materials (carbon textiles and epoxy resin) were presented. An analytical load transfer model was developed and the results compared to the experimental data in term of reinforcement longitudinal strains and interfacial shear stresses. The experimental results by the authors were combined to 81 experimental data selected from the literature in order to get an enlarged extensive database consisting of 109 push–pull shear tests. An analytical bond strength model was introduced and the relevant parameters were statistically calibrated on the basis of the enlarged database. In particular, a statistical analysis of the fracture energy parameter, k_G, was performed and the experimental data were fitted under the assumption of both normal and lognormal distribution. Experimental and analytical results show that:

1. A significant scatter of the experimental results was observed. This is probably due to the sensitivity of the reinforcement system to the detailing of the experimental setup. In particular the debonding load is sensitive to the axial alignment with the applied load and in some cases debonding tends to be of mixed mode due to the presence of out of plane displacement. Also the surface preparation plays an important role in the debonding strength but in the present experimental work no specific surface preparation or primer application was considered.
2. Statistical analysis shows that the normal distribution model produces an accurate estimation of the debonding load and a lognormal statistical model is not required.
3. The adopted bond strength model appears to fit well the experimental data for a large set of reinforcement length and width. With reference to the clay brick compressive strength, the model are able to capture the trend for compressive strength values ranging from, approximately, 10 MPa to 70 MPa.

Additional experimental activities are finally required in order to investigate the effect of surface preparation (roughness) including the influence of a primer application and the presence of mortar layers on the debonding load.

Acknowledgements

The experiments described in this paper were developed at the Material Testing Laboratory of the Politecnico di Milano. The financial support of the Politecnico di Milano is gratefully acknowledged. Thanks are also expressed to Sika Italia S.p.A. for providing the reinforcing materials used in the experimental campaign.

References

[1] Sciolti MS, Aiello MA, Frigione M. Influence of water on bond behavior between CFRP sheet and natural calcareous stones. Compos Part B 2012;43:3239–50.
[2] Cromwell JR, Harries KA, Shahrooz BM. Environmental durability of externally bonded FRP materials intended for repair of concrete structures. Constr Build Mater 2011;25:2528–39.
[3] Binda L, Tedeschi C, Valluzzi MR, Garbin E, Panizza M. Salt crystallization tests on brick masonry reinforced by CFRP textiles. In: 12th international conference on durability of building materials and components (XII DBMC). Porto (Portugal); 12–15 April 2011.
[4] Valluzzi MR, Garbin E, Panizza M, Binda L, Tedeschi C. Moisture and temperature influence on FRP masonry bonding. In: 12th international conference on durability of building materials and components (XII DBMC). Porto (Portugal); 12–15 April 2011.
[5] Bilotta A, Di Ludovico M, Nigro E. FRP-to-concrete interface debonding: experimental calibration of a capacity model. Compos Part B 2011;42:1539–53.
[6] Valluzzi MR, Tinazzi D, Modena C. Shear behavior of masonry panels strengthened by FRP laminates. Constr Build Mater 2002;16:409–16.
[7] CNR-DT 200 R1/2013. Istruzioni per la progettazione, l'esecuzione e il controllo di interventi di consolidamento statico mediante l'utilizzo di compositi fibrorinforzati. Materiali, strutture di c.a. e di c.a.p., strutture murarie. Italian national research council; 2013.
[8] Colombi P, Fava G, Poggi C. End debonding of CFRP wraps and strips for the strengthening of concrete structures. Compos. Struct. 2014;111(1):510–21.
[9] Briccoli Bati S, Fagone M. An analysis of CFRP-brick bonded joints. In: Proceedings of the XVIII conference of the italian group of computational mechanics (GIMC/XVIII), Siracusa (Italy); 22–24 September 2010.
[10] Aiello MA, Sciolti SM. Bond analysis of masonry structures strengthened with CFRP sheets. Constr Build Mater 2006;20:90–100.
[11] Capozucca R. Experimental FRP/SRP-historic masonry delamination. Compos Struct 2010;92:891–903.
[12] Kwiecien A. Stiff and flexible adhesive bonding CFRP to masonry substrates investigated in pull-off test and single-lap shear test. Mech. Eng. 2012;12:228–39.
[13] Valluzzi MR et al. Round Robin test for composite-to-brick shear bond characterization. Mater Struct 2012. http://dx.doi.org/10.1617/s11527-012-9883-5.
[14] Ceroni F, Ferracuti B, Pecce M, Savoia M. Assessment of a bond strength model for FRP reinforcement externally bonded over masonry blocks. Compos Part B 2014;61:147–61.
[15] Ferracuti B, Savoia M, Mazzotti C. Interface law for FRP-concrete delamination. Compos Struct 2007;80:523–31.
[16] Carozzi FG, Milani G, Poggi C. Mechanical properties and numerical modeling of fabric reinforced cementitious matrix (FRCM) systems for strengthening of masonry structures. Compos Struct 2014;107:711–25.
[17] Carozzi F.G., Colombi P., di Feo C., Montalbano A., Poggi C. The use of GFRP grids for structural rehabilitation of masonry elements. In: Proceedings of the 6th international conference on FRP composite in civil engineering (CICE 2012), Rome, Italy; 13–15 June 2012.
[18] ASTM D3039/2008 Standard test method for tensile properties of polymer matrix composite materials. Am Soc Test Mater 2008.
[19] ASTM D638/2003 Standard test method for tensile properties of plastics. Am Soc Test Mater 2003.
[20] EN 14580/2005 Natural stone test methods – Determination of static elastic modulus. UNI standard; 2005.
[21] EN 772-1/2011 Methods of test for masonry units – determination of compressive strength. UNI standard; 2011.
[22] EN 1015-18/2004 Methods of test for mortar of masonry - determination of water absorption coefficient due to capillary action of hardened mortar. UNI standard; 2004.
[23] EN 1542/2000 Products and system for the protection and repair of concrete structures – test methods – measurement of bond strength by pull-off. UNI standard; 2000.
[24] Pazmino J, Carvelli V, Lomov SV, Van Mieghem B, Lava P. 3D digital image correlation measurements during shaping of a non-crimp 3D orthogonal woven E-glass reinforcement. Int J Mater Form 2013. http://dx.doi.org/10.1007/s12289-013-1139-6.
[25] Ghiassi B, Xavier J, Oliveira DV, Lourenco PB. Application of digital image correlation in investigating the bond between FRP and masonry. Compos Struct 2013;106:340–9.
[26] Capozucca R. Behaviour of CFRP sheets bonded to historical masonry. In: Smith ST, editor. Proceedings of asia-pacific conference on FRP in structures (APFIS 2007), Hong Kong (China); 12–14 December 2007.
[27] Lu XZ, Teng JG, Ye LP, Jiang JG. Bond-slip models for FRP sheets/plates bonded to concrete. Eng Struct 2005;27(4):920–37.